Fast time variations of supernova neutrino fluxes and their detectability

Tina Lund,[1] Andreas Marek,[2] Cecilia Lunardini,[3,4] Hans-Thomas Janka,[2] and Georg Raffelt[5]

[1]*Department of Physics and Astronomy, Aarhus University, Ny Munkegade 120, 8000 Aarhus C, Denmark*
[2]*Max-Planck-Institut für Astrophysik, Karl-Schwarzschild-Str. 1, 85748 Garching, Germany*
[3]*Arizona State University, Tempe, AZ 85287-1504, USA*
[4]*RIKEN BNL Research Center, Brookhaven National Laboratory, Upton, NY 11973, USA*
[5]*Max-Planck-Institut für Physik (Werner-Heisenberg-Institut), Föhringer Ring 6, 80805 München, Germany*

(Dated: 18 August 2010)

In the delayed explosion scenario of core-collapse supernovae (SNe), the accretion phase shows pronounced convective overturns and a low-multipole hydrodynamic instability, the standing accretion shock instability (SASI). These effects imprint detectable fast time variations on the emerging neutrino flux. Among existing detectors, IceCube is best suited to this task, providing an event rate of ~ 1000 ms^{-1} during the accretion phase for a fiducial SN distance of 10 kpc, comparable to what could be achieved with a megaton water Cherenkov detector. If the SASI activity lasts for several hundred ms, a Fourier component with an amplitude of 1% of the average signal clearly sticks out from the shot noise. We analyze in detail the output of axially symmetric hydrodynamical simulations that predict much larger amplitudes up to frequencies of a few hundred Hz. If these models are roughly representative for realistic SNe, fast time variations of the neutrino signal are easily detectable in IceCube or future megaton-class instruments. We also discuss the information that could be deduced from such a measurement about the physics in the SN core and the explosion mechanism of the SN.

PACS numbers: 14.60.Pq, 97.60.Bw

arXiv:1006.1889v2 [astro-ph.HE] 23 Aug 2010

I. INTRODUCTION

The delayed explosion scenario remains the standard paradigm for the core collapse supernova (SN) mechanism. After core bounce a shock wave forms that stalls at a typical radius of 100–200 km while matter keeps falling in, forming a standing accretion shock that can last for several hundred ms before the shock is re-launched, presumably after sufficient neutrino energy deposition in the region behind the shock. Two- and three-dimensional hydrodynamic simulations reveal convective instabilities that quickly develop into large-scale convective overturns and a strong dipole oscillation of the neutron star against the "cavity" formed by the standing shock, the standing accretion shock instability (SASI) [1–7].

During the accretion phase, neutrino emission is particularly large, being powered primarily by the gravitational energy of the in-falling material. In the SASI scenario the neutrino emission is strongly modulated. As an example we show in Fig. 1 the $\bar{\nu}_e$ luminosity as a function of time, averaged over one hemisphere, from the two-dimensional simulations of Marek, Janka and Müller (2009) [6]. As noted by these authors, such large flux variations could well become detectable in the high-statistics neutrino signal of the next galactic SN, revealing direct evidence for the predicted SASI mode and convective overturns.

The detection of fast time variations, or equivalently, identifying high-frequency Fourier modes in the signal, is limited by the number of registered events: A significant signal must stick above the shot noise caused by the fluctuating event rate, so a large counting rate is crucial. Among the existing or near-future detectors, IceCube is the most promising because it detects a large number of Cherenkov photons triggered by neutrinos. At most one single Cherenkov photon is picked up from a given neutrino, so every photon tags the arrival time of a different neutrino. For our SN example of Fig. 1, assumed at a fiducial distance of 10 kpc, the maximum photon detection rate is roughly 1000 ms^{-1}, similar to the intrinsic background rate. On the other hand, for Super-Kamiokande (fiducial volume 22.5 kt) the corresponding neutrino detection rate is approximately two orders of magnitude smaller, although essentially background free. Based on this simple estimate, we use IceCube as our benchmark detector. On the other hand, a megaton-class water Cherenkov detector would achieve neutrino detection rates similar to IceCube and in addition would provide event-by-event energy information, a quantity also showing strong fluctuations. The potential of such a detector will be studied elsewhere.

A possible limiting factor to detecting fast signal variations is time-of-flight dispersion caused by neutrino masses. The delay of arrival times is

$$\Delta t = 0.57 \text{ ms} \left(\frac{m}{\text{eV}}\right)^2 \left(\frac{30 \text{ MeV}}{E}\right)^2 \left(\frac{D}{10 \text{ kpc}}\right)^2 . \quad (1)$$

We will see that signal variations may be detectable up to a few hundred Hz, corresponding to time scales of several ms. So even for eV neutrino masses, arrival time dispersion would be a marginal effect. Moreover, current cosmological limits on the overall neutrino mass scale are approximately 0.2 eV [8], very similar to the sensitivity of the ongoing KATRIN experiment [9]. Assuming KATRIN will confirm this limit, arrival time dispersion of SN neutrinos will be completely irrelevant in our context. Should KATRIN discover eV-scale neutrino masses

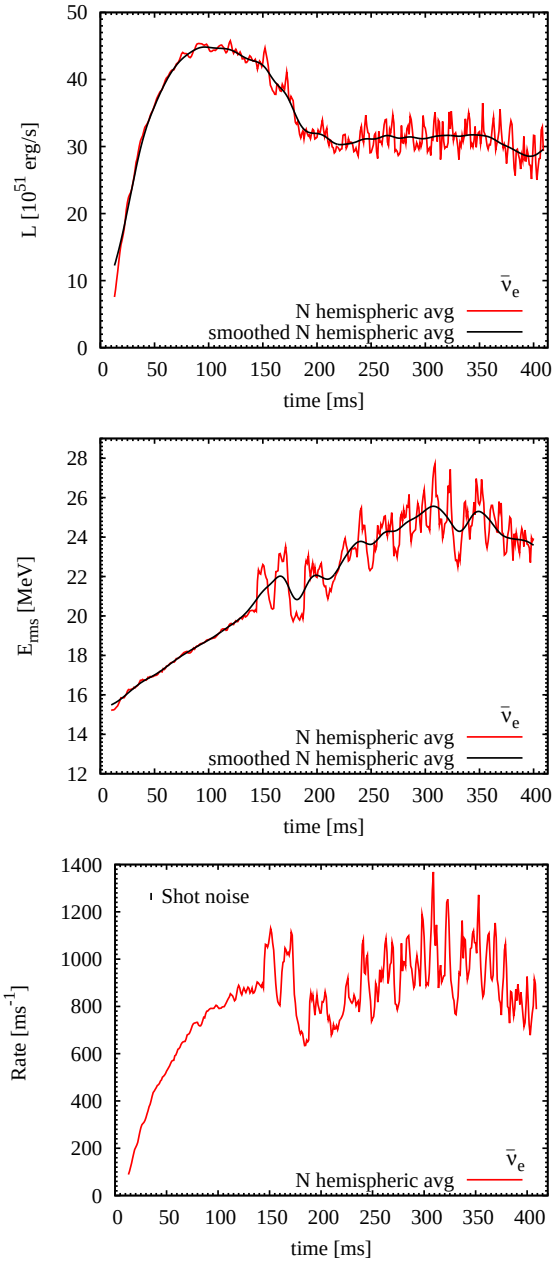

FIG. 1: *Top:* $\bar{\nu}_e$ luminosity of our baseline SN model sampled at 1 ms intervals. Red line: North hemispheric average. Black line: Moving average with a Gaussian window function (σ = 7 ms). *Middle:* $\bar{\nu}_e$ rms energy. Red and black lines as the panel above. *Bottom:* Detection rate in IceCube. Also shown is the $1\,\sigma$ range caused by shot noise, assuming a bin width of 1 ms.

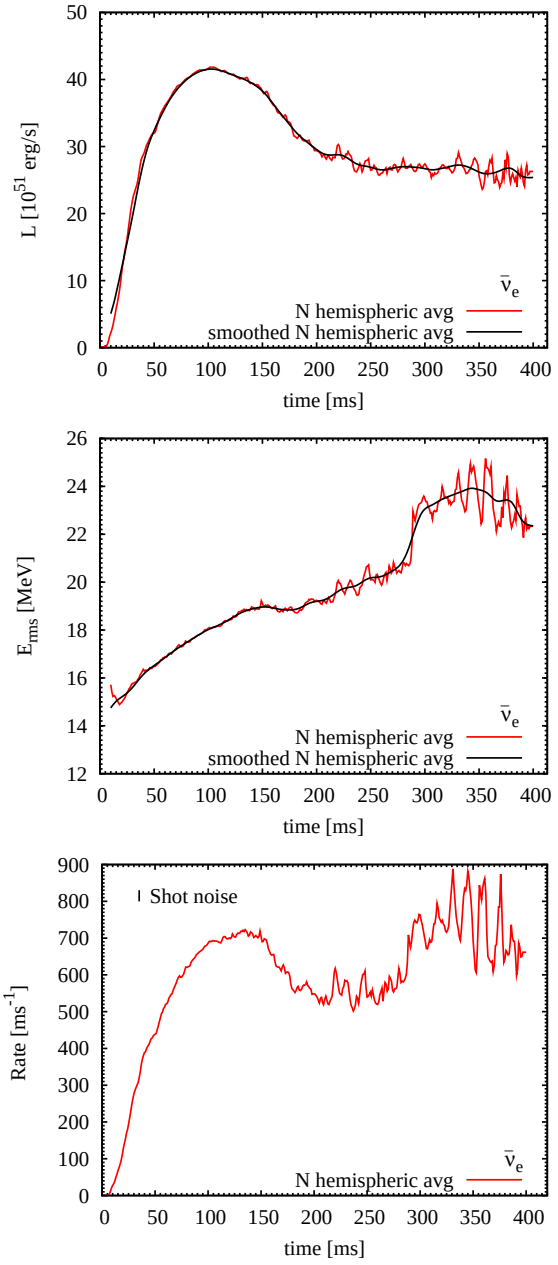

FIG. 2: Same as Fig. 1 using the EoS of Hillebrandt and Wolff.

in violation of cosmological limits one could return to this study and include time-of-flight dispersion.

In Sec. II we review the detector response of IceCube to SN neutrinos. In Sec. III we use the output from the numerical models of Marek, Janka and Müller (2009) [6] and study the signal power as a function of frequency relative to the detector shot noise. In Sec. IV we briefly discuss the fluctuations of neutrino energies relative to luminosity variations. In Sec. V we consider the modification caused by a stiffer nuclear equation of state. In Sect. VI we interpret the results of our analysis on the basis of present explosion models and our understanding of the physics relevant in the SN core. We also briefly address the question what could be learned if SASI and convective neutrino signal variations were detected. We discuss and summarize our findings in Sec. VII. In Appendix A we derive the detector shot noise and define the normalization of our Fourier transform of binned data.

II. DETECTOR MODEL

The IceCube detector, soon to be completed at the South Pole, currently provides by far the largest detection rate for the next nearby SN. For our sensitivity forecast we use a somewhat schematic model for its response to a SN neutrino signal. For the finished detector with 4800 optical modules, the latest efficiencies provide a detection rate of Cherenkov photons originating from the dominant inverse beta reaction $\bar\nu_e + p \to n + e^+$ of [10–12]

$$R_{\bar\nu_e} = 114\ \mathrm{ms}^{-1}\,\frac{L_{\bar\nu_e}}{10^{52}\ \mathrm{erg\ s}^{-1}}\left(\frac{10\ \mathrm{kpc}}{D}\right)^2\left(\frac{E_{\rm rms}}{15\ \mathrm{MeV}}\right)^2. \tag{2}$$

Here we use the definition

$$E_{\rm rms}^2 = \frac{\langle E^3\rangle}{\langle E\rangle}\,, \tag{3}$$

where the average is to be taken over the neutrino distribution function. This quantity plays the role of an rms energy relative to the energy spectrum, not the flux spectrum. Other authors use the definition $E_{\rm rms} = \sqrt{\langle E^2\rangle}$, which is perhaps more appropriately called the rms energy, but our definition is what appears in the IceCube rate and thus will be used. In other words, because the Cherenkov light measures the neutrino energy deposition in ice, $L_{\bar\nu_e}$ and $E_{\rm rms}$ are the most natural parameters to describe the instantaneous neutrino flux. Our estimate of the photon count rate Eq. (2) uses an approximate inverse beta cross section of $\sigma = 9.52\times10^{-44}\ \mathrm{cm}^2\,(E_{\bar\nu_e}/\mathrm{MeV})^2$ to obtain a simple scaling behavior with energy.

For low-energy neutrino detection, IceCube is a very coarse detector, implying that from a given neutrino it picks up at most one Cherenkov photon. Assuming more closely spaced optical modules, the average photon detection rate remains unchanged, but the fluctuations increase in that several detected photons may have been triggered by the same neutrino. This increased shot noise reduces the capability to detect fast time variations. In the extreme case of a densely instrumented detector such as Super-Kamiokande, one measures so many photons from a given neutrino that one can reconstruct detailed energy and directional information, at the expense of relatively few neutrino events and therefore much larger shot noise. In this sense the apparent weakness of IceCube for low-energy neutrino detection is actually a virtue for diagnosing fast time variations. Since for IceCube a single photon detection is identical with detecting the arrival time of a neutrino (except for background), we use the term "event" interchangeably for "photon detection" or "neutrino detection."

For our SN models, a typical rate during the accretion phase is around $10^3\ \mathrm{ms}^{-1}$. This is to be compared with the estimated IceCube background rate of [11]

$$R_{\rm bkgd} = 1.34\times10^3\ \mathrm{ms}^{-1}\,. \tag{4}$$

This is the dark current of $280\ \mathrm{s}^{-1}$ per optical module, multiplied with 4800 optical modules of the final detector to be completed by the end of this year. Therefore, for a SN at the fiducial distance, the signal and background rates are comparable, but the background dominates. Therefore, it is essentially the shot noise of the background that limits the detectability of fast signal variations unless the SN is closer.

IceCube samples the data in 1.6384 ms bins whereas low-energy water Cherenkov or scintillator detectors register the times t_j of every event with high precision. The bin width, or the absence of binning, only affects the sensitivity to frequencies that we will see are too high to be detected. Therefore, the details of signal binning do not enter our discussion. We have found it convenient to use 1 ms as a nominal bin width and also as a sampling rate of the numerical SN results.

The main obstacle to detecting fast time variations is shot noise (Poisson fluctuations of the limited number of events). In the lower panel of Fig. 1 we show as a vertical bar the $1\,\sigma$ fluctuation per 1 ms bin for an event rate of $900\ \mathrm{ms}^{-1}$. Therefore, it is evident that with IceCube one can follow the overall neutrino light curve with excellent precision.

To estimate the required amplitude for a fast periodic variation to be detectable, we model the signal as a sequence of arrival times t_j with $j = 1,\ldots,N$. The Fourier transform of this signal (frequency f) is

$$g(f) = \sum_{j=1}^{N} \mathrm{e}^{-\mathrm{i}2\pi f t_j} \tag{5}$$

with the spectral power $G(f) = |g(f)|^2$. The detection rate has units of inverse time, so the Fourier components are dimensionless. If the sequence of events is completely random, i.e. the times t_j sample a uniform distribution on a given time interval, one can show (Appendix A) that

$$\frac{\langle G_{f\neq0}\rangle}{G_{f=0}} = \frac{1}{N} \tag{6}$$

and we note that $G(0) = N^2$.

Next we assume the signal has a frequency f_a imprinted upon it, i.e. it is proportional to $[1+a\cos(2\pi f_a t)]$. The power of this signal vanishes everywhere except at $f = 0$ and $f = \pm f_a$. The relative power is $G(\pm f_a)/G(0) = a^2/4$. Therefore, an imprinted cosine variation with the amplitude $a = 2/\sqrt{N}$ is equal to the shot noise. Assuming that the accretion phase lasts for 400 ms and using the background rate of Eq. (4) as the dominant source of shot noise, the number of events is $N = 5.4\times10^5$ and the shot-noise level corresponds to a cosine amplitude of $a = 3\times10^{-3}$. Of course, to stick reliably above background, a Fourier component would need to be somewhat larger. In other words, for a SN at 10 kpc one can expect to detect signal variations with an amplitude roughly on the 1% level of the average rate. The signal variations shown in the lower panel of Fig. 1 would easily show up in IceCube.

III. NUMERICAL SUPERNOVA SIGNAL

A. Description of the model

To make this rough estimate more concrete, we next use a numerical simulation to compare the expected signal fluctuations with the sensitivity of IceCube. The two-dimensional (axially symmetric) simulations which this discussion is based on were performed with the Prometheus-Vertex Code [13, 14] and the simulations were already discussed in detail in Ref. [6]. We therefore repeat only a few essential aspects of both the numerical treatment and the simulation runs and refer to Refs. [5, 6] for more complete information.

The hydrodynamic part of the code is based on a conservative and explicit Eulerian implementation of a Godunov-type scheme with higher-order spatial and temporal accuracy. It solves the nonrelativistic conservation equations for the stellar fluid, whose self-gravity is described by an "effective relativistic potential" [15]. It provides a sufficiently accurate approximation of general relativistic corrections [16].

The neutrino transport solver, which is coupled to the hydrodynamics module via lepton number, energy and momentum source terms, is computed with a "ray-by-ray plus" scheme [14]. It accounts for the full neutrino-energy dependence in the transport but assumes the neutrino flux at every point to be radial (i.e. the neutrino phase space distribution function is assumed to be axially symmetric around the radial direction), which is numerically less demanding and more efficient than a full multi-dimensional version of the transport.

The simulations used here are based on the progenitor model s15s7b2 from Woosley and Weaver [17], and is representative for the collapse of stars with progenitor masses around $15\,M_\odot$. The dense proto-neutron star matter is described by the equation of state (EoS) of Lattimer and Swesty [18], which leads to a radius of 12 km for a cold neutron star with a gravitational mass of $1.4\,M_\odot$. We also consider briefly an example with the EoS of Hillebrandt and Wolff that is considerably stiffer [19]. Unless otherwise noted, our discussion always refers to the Lattimer and Swesty case as a benchmark.

The two-dimensional model was computed under the assumption of axial symmetry and covers the region between north and south pole with 192 equally spaced angular grid points. The model was evolved in total for about 600 ms from the onset of the collapse to a time of about 450 ms after the formation of the SN shock front and shows in the postbounce evolution a strong SASI sloshing activity of the SN shock front.

The oscillations of the SN shock front due to SASI activity and convective overturn cause luminosity fluctuations by modulating the mass accretion on the proto-neutron star: a strong shock retraction leads to a transient increase of the gas flow towards the neutron star and to the compression and enhanced cooling of the matter (i.e. enhanced neutrino emission) near the neutron star surface [6]. On the other hand, a shock expansion has the opposite effect because it causes a deceleration of the infall or even outward acceleration of material that is accreted through the shock front. Thus shock expansion stretches the time this matter stays in the gain layer and less cooling by neutrino emission occurs.

From the 192 angular rays of the models, we used in the post processing the luminosity for all species ν_e, $\bar{\nu}_e$ and ν_x and the corresponding $\langle E\rangle_{\rm rms}$ on every second angular bin and extracted the information in steps of about 0.5 ms that were subsequently resampled in exact 1 ms steps. To illustrate the general appearance and directional differences of the fluctuations, we combined the angular rays into 5 directional averages: North polar, equatorial, south polar, and an intermediate wedge between each pole and equator, each of them covering a zenith-angle range of 36°. For $\bar{\nu}_e$, the luminosity, rms energy and IceCube detection rate of the 5 wedges are shown in Fig. 3. Of course, these plots have no direct observational significance and merely serve to illustrate the angular variation of the SN output. We clearly see that fluctuations in the energy and luminosity are larger along the polar directions than at the equator. In Fig. 4 we show the same information for the run with the EoS of Hillebrandt and Wolff, on which we will comment later.

B. Fourier transform and spectral power

In order to assess the detectability of such fluctuations we calculate the Fourier transform of the detection rate, at first for the run with the Lattimer and Swesty EoS. To simplify this process we have resampled the data in exact 1 ms intervals over a range of 400 ms, discarding a few ms of data at the beginning and end of the original sequence that covered the interval 10.5 ms to 417 ms post bounce. We take the Fourier transform on the full 400 ms interval, however applying a Hann window function to reduce edge effects (Appendix A). From Fig. 3 it is apparent that fast time variations commence in earnest at about 150 ms postbounce and we could have left out the initial phase of the signal to reduce the number of background events within the signal region. On the other hand, the window function anyway suppresses the signal portion at the edges and so we have kept the full 400 ms range.

The power spectra are in absolute units, not relative to the average signal. In our normalization the Fourier amplitude at $f = 0$ is $N_{\rm events}/N_{\rm bins}$, i.e. the average rate per bin (Appendix A). In this way the average power does not change if we consider sub–samples of the data for a shorter duration, keeping the individual bin width fixed. The power at $f = 0$ is therefore $(N_{\rm events}/N_{\rm bins})^2$. Since a typical event rate is $1000\ {\rm ms}^{-1}$ and our bin width is 1 ms, the power spectrum at $f = 0$ is around 10^6 and much smaller at other frequencies. Using a 400 ms time interval implies that the natural frequency spacing is 2.5 Hz, and based on our 1 ms binning the largest frequency that can be resolved is 500 Hz (Nyquist frequency).

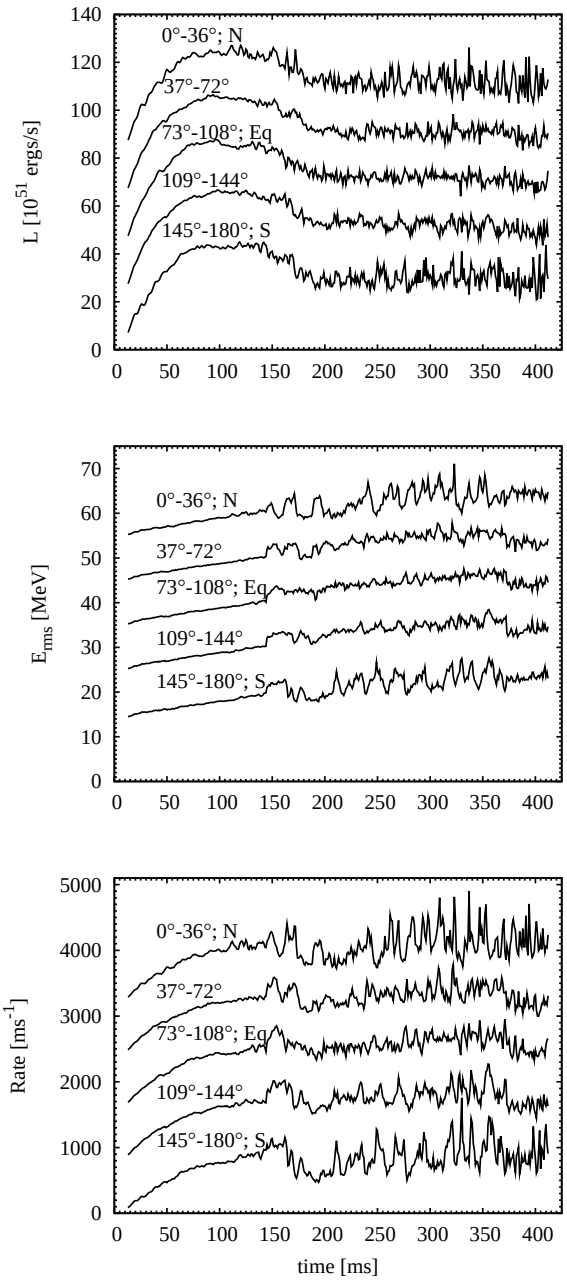

FIG. 3: Luminosity, rms energy and IceCube event rate based on the $\bar{\nu}_e$ fluxes of our model with Lattimer and Swesty EoS. The 96 angular rays have been combined into five averages ranging from north (top curve) to south (bottom curve), where in each panel the curves are offset relative to each other by 20, 10 and 800 units of the vertical axes, respectively.

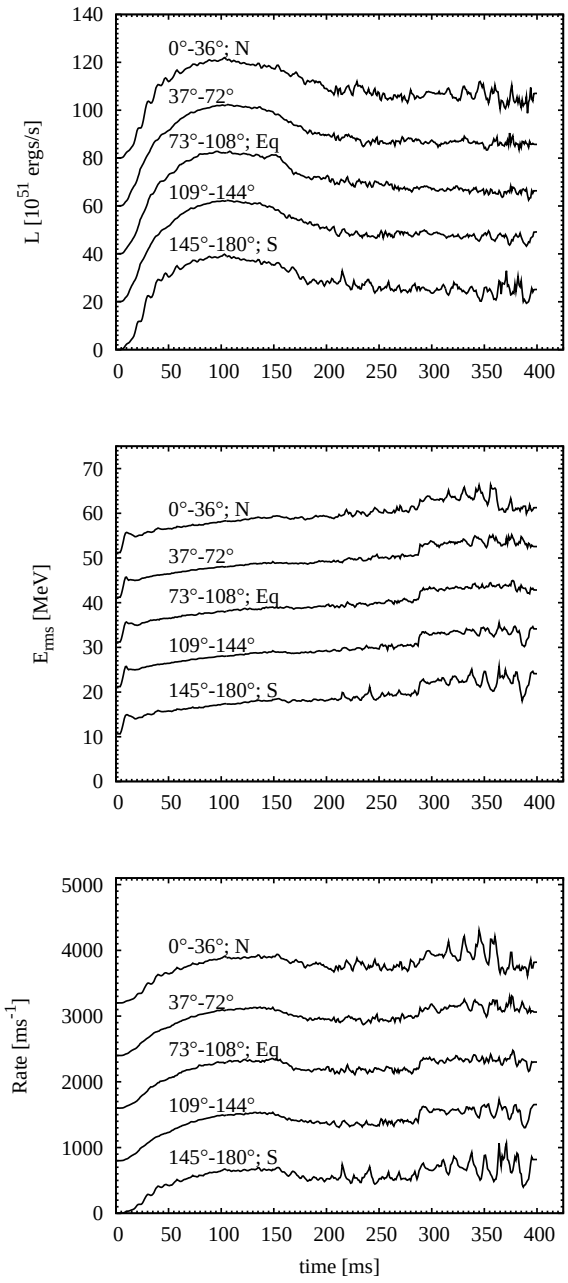

FIG. 4: Same as Fig. 3 for a run with the EoS of Hillebrandt and Wolff.

Based on the background rate of Eq. (4), a signal duration of $\tau = 400$ ms and a Hann window function, the shot noise power of the detector dark current is given in Eq. (A12) and is found to be 10.08 in the described units where the zero-frequency power is $(N_{\rm events}/N_{\rm bins})^2$. In the subsequent plots this power level is shown as a horizontal grey line.

The modification of our power spectra plots as a function of SN distance D is not entirely trivial. If the SN is further away than 10 kpc, we lose event rate quadratically with distance. Since we are showing the power spectrum, another power of 2 arises. Therefore, relative to the fixed IceCube dark current (the horizontal line), the power spectra are lowered by a factor $(10\ {\rm kpc}/D)^4$. The distance distribution of galactic SNe is very broad, but declines quickly beyond about 20 kpc [20]. At this pessimistic distance, the signal power spectrum would be lowered by a factor of 16, whereas the shot noise level would remain fixed.

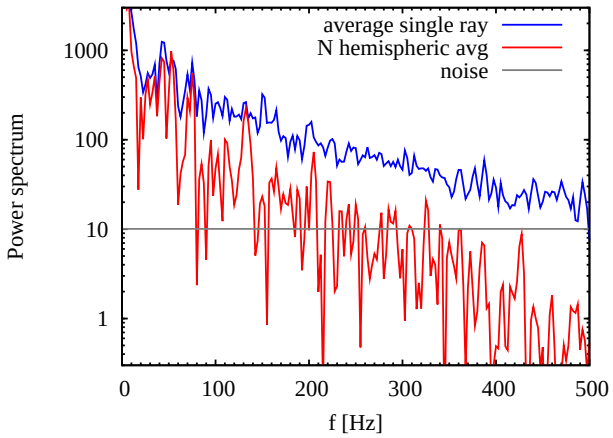

FIG. 5: Power spectrum of the IceCube event rate for our model (EoS of Lattimer and Swesty) in 2.5 Hz increments. Blue line (upper curve): Average single-ray power spectrum. Red line (lower curve): northern hemispheric average. Horizontal line: Shot noise from IceCube dark current.

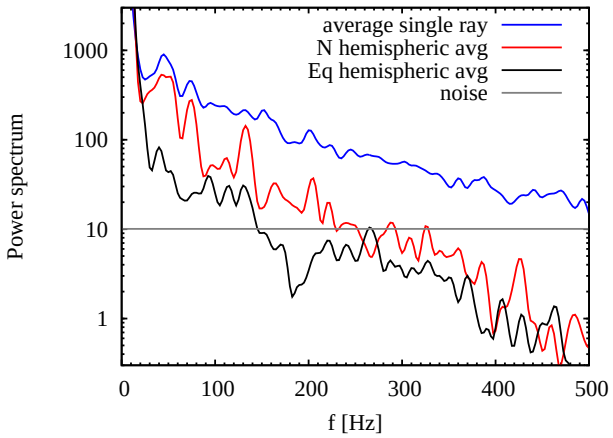

FIG. 6: Same as Fig. 5 with smoothing by a moving average with a Gaussian window function of width $\sigma = 4$ Hz. Average power of all 96 single rays (blue), northern hemispheric average (red), and equatorial hemispheric average (black), from top to bottom.

On the other hand, if the SN is closer than 10 kpc, the IceCube dark current quickly becomes irrelevant. The shot noise is determined by the number of detected SN events which increases with decreasing distance as $(10\ \mathrm{kpc}/D)^2$ and therefore the shot-noise level increases with this factor. The signal power spectrum increases with the fourth power $(10\ \mathrm{kpc}/D)^4$ as before, so relative to the shot-noise level the signal power increases quadratically with decreasing distance as $(10\ \mathrm{kpc}/D)^2$.

C. Hemispheric averaging

As a first example we show in Fig. 5 as a blue line (upper curve) the power spectrum of the event rate based on a single ray. To this end we have taken an ensemble average of the power spectra of all 96 angular rays with equal weights, treating each one as if it were responsible for the full 4π neutrino emission and thus for the full detector signal. Taking a true single ray instead of an ensemble average shows the same trend with much greater noise and of course with directional differences. (Such a single-ray treatment would correspond to the assumption that all neutrinos are emitted strictly in the radial direction and the observer receives neutrinos just from one spot on the stellar surface.) Up to the Nyquist frequency of 500 Hz the single-ray power stays far above the background and thus would be clearly detectable.

The true signal is caused by the integrated emission over the hemisphere facing the detector. In principle, it could be reconstructed from the detailed angular information of the neutrino emission as provided by our numerical solution of the neutrino transport. However, in view of the approximative nature of 2D models and of the "ray-by-ray plus" transport treatment (see Sec. III.A) we preferred to avoid processing the huge amount of corresponding data. As a simplification we assumed that each surface element radiates isotropically with an energy spectrum according to the local conditions. In other words, we added the computed local fluxes, weighted by the projected area of the surface elements as seen by the observer. Taking the northern hemispheric average in this sense leads to the red (lower) curve in Fig. 5.

The spectral power declines much faster with increasing frequency than in the single-ray case. This is expected because high-frequency luminosity variations are due to small spatial scales of the "boiling" medium whereas the lowest frequencies are due to the largest-scale convective overturns and SASI activity. The variations on small spatial scales are not strongly correlated and therefore reduced when taking an average over the entire hemisphere whereas the large-scale motions are correlated and not averaged away.

The hemispheric power spectrum is quite noisy and the overall trend is better seen in a smoothed version shown in Fig. 6. Here we show the same information based on a moving average with a Gaussian window function with $\sigma = 4$ Hz. In addition we show the equatorial average as a black curve. It is the lowest curve and has significantly less power than the northern case (which is similar to the southern one). In this simulation the large-scale motion is essentially along the symmetry axis of the simulation, explaining much larger luminosity variations in the polar directions than the equatorial one. Indeed, the luminosity and temperature variations in the north and south are anti-correlated because of the dipole nature of the SASI oscillation, so in the equatorial view the variations largely cancel. In a realistic 3-D situation, the dipole direction is not necessarily fixed in space, so over several hundred ms the average view from different directions probably would not differ as dramatically as in this axisymmetric simulation.

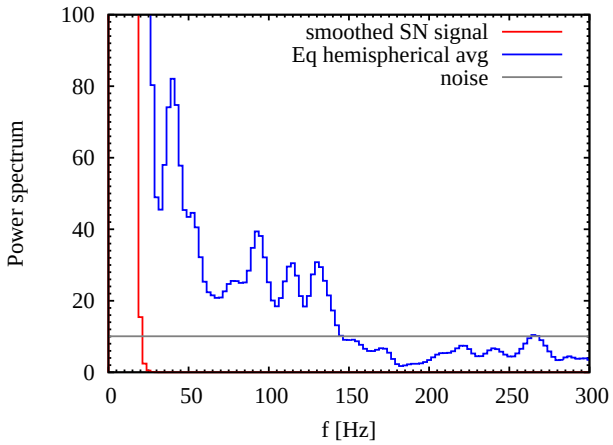

FIG. 7: Comparison between fluctuating and smooth signal for the model with Lattimer and Swesty EoS. Blue: Power spectrum of equatorial hemispheric average signal. Red: Same for smoothed SN signal.

D. Comparison with spherically symmetric case

An important issue is how well one can distinguish the signal from a spherically symmetric model from a convecting one. To this end we have produced an equivalent spherically symmetric model by smoothing the output from our model by a moving average. An example for the corresponding smooth luminosity is shown in Fig. 1. We compare the signal power spectrum for the equatorial hemispheric average in Fig. 7 with that from a smoothed version of this average. We see that the smooth signal plummets below the IceCube background noise level at around 20 Hz. In other words, for the case studied here the power spectrum roughly above 20 Hz is a clear indication for fast time fluctuations of the neutrino source.

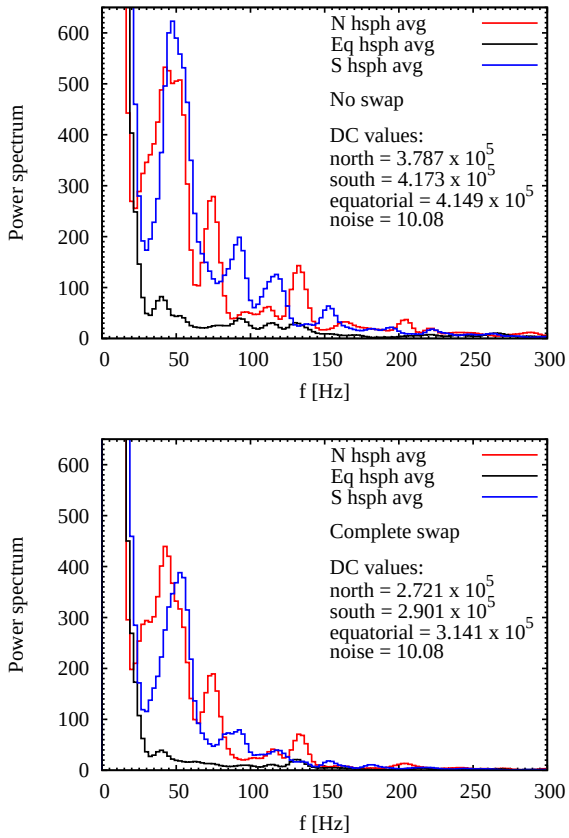

FIG. 8: Smoothed power spectrum of the event rate for the northern (red), equatorial (black) and southern (blue) hemispheric averages (EoS of Lattimer and Swesty). The shot noise level of the background is at 10.08. *Top:* No flavor oscillations. *Bottom:* Complete swap $\bar{\nu}_e \leftrightarrow \bar{\nu}_x$. In the panels we also give the DC values, i.e. the power at zero frequency, corresponding to $(N_{\rm events}/N_{\rm bins})^2$.

E. Directional and flavor dependence

For a more detailed appreciation we next show in Fig. 8, upper panel, the smoothed power spectrum for the northern, southern and equatorial average signals. We first observe that from ∼20 Hz to ∼175 Hz for $\bar{\nu}_e$ the power spectrum for all three hemispheric averages are comfortably above the noise level in IceCube. We furthermore see that the first peak for both polar directions are roughly coinciding, and although the specific pattern differs at larger frequencies the levels are comparable. The pronounced peak at 50 Hz corresponds to variations with a 20 ms period. This period is easily seen in Fig. 5 of Ref. [6] where the dipole motion of the shock-wave surface is plotted.

In the lower panel we show the same signal under the assumption that complete flavor transformations have taken place and what reaches IceCube are $\bar{\nu}_e$ that at the SN were born as $\bar{\nu}_x$. The qualitative features are similar as before. In other words, full or partial flavor transformations would not change the picture substantially. The overall power spectrum is now slightly lower. However, this effect is due to the reduced $\bar{\nu}_x$ luminosity during the accretion phase relative to the $\bar{\nu}_e$ luminosity. In the figure panels we give the DC ("direct current") values of the power spectrum, i.e. the power at zero frequency which is significantly larger in the $\bar{\nu}_e$ case (upper panel). In other words, the *relative* fluctuation amplitude is similar for both species.

The same information is given in Fig. 9 where we show the equatorial average (top panel) and northern average (bottom) and each time compare the $\bar{\nu}_e$ signal with the case of complete flavor swap. Especially the northern case (very similar to the southern one) shows that flavor transformations have little impact on the interpretation of fast signal variations.

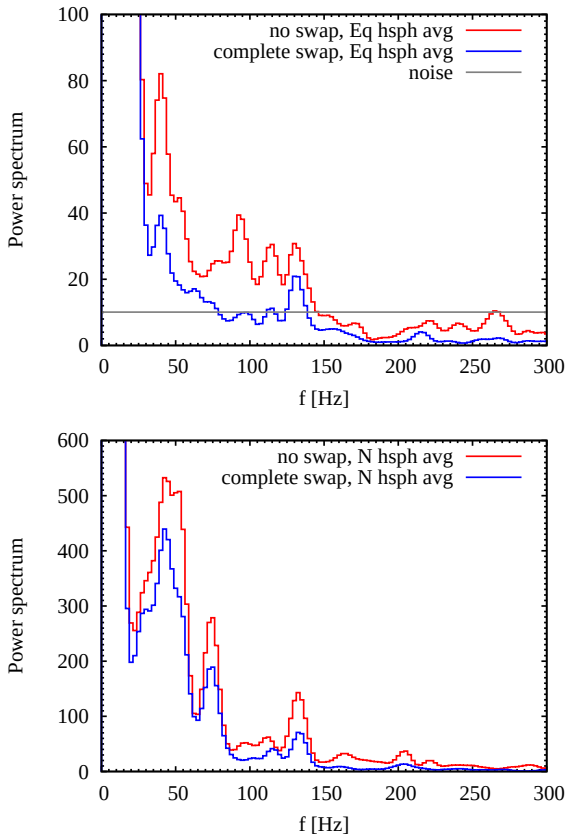

FIG. 9: Comparing no oscillations (red) with complete flavor swap (blue) for the model with Lattimer and Swesty EoS. *Top:* equatorial. *Bottom:* northern.

IV. LUMINOSITY VS. ENERGY FLUCTUATIONS

Thus far we have focussed on the counting-rate fluctuations in IceCube because among existing detectors it provides by far the largest event rate. With a future megaton-class water Cherenkov detector the picture would change because the event rate would be comparable to IceCube and in addition one would obtain event-by-event energy information. In this case spectral fluctuations would become important as well.

In Fig. 1 it is apparent that the IceCube signal variations are much larger than the luminosity variations. The fluctuations of $E_{\rm rms}$ must be responsible for the difference. Moreover, one expects that the spectral fluctuations are correlated with the luminosity fluctuations so that both effects interfere constructively.

To quantify these arguments we consider as a specific example the northern hemispheric average of the luminosity $L(t)$ and the rms energy $E_{\rm rms}(t)$ and their correlation. Since we are here concerned with the IceCube signal, that is proportional to $E^2_{\rm rms}$, we consider the two functions $L(t)$ and $W(t) = E^2_{\rm rms}(t)$. For convenience we normalize them somewhat arbitrarily to their average values over the 274–400 ms interval since now we are primarily interested in relative fluctuations. (Our conclusions do not change much if we normalize to the average values over the entire 400 ms interval.) We next calculate the Fourier transforms $\tilde{L}$ and $\tilde{W}$ of these dimensionless functions. In the upper panel of Fig. 10 we show the power spectra. The spectral power of W is significantly larger than that of L, i.e. the IceCube signal variations are dominated by $E^2_{\rm rms}$ variations.

To quantify correlations between spectral and luminosity variations we show in the lower panel of Fig. 10 the quantities $|\tilde{W}|\,|\tilde{L}|$ and $\frac{1}{2}(\tilde{W}^*\tilde{L} + \tilde{W}\tilde{L}^*)$. The two quantities are similar and the correlation function is positive almost everywhere, so indeed $W(t)$ and $L(t)$ are strongly correlated.

These results suggest that energy- and event-rate fluctuations and their correlation, that could be measured in a megaton water Cherenkov detector, would provide additional signatures for convection and SASI activity.

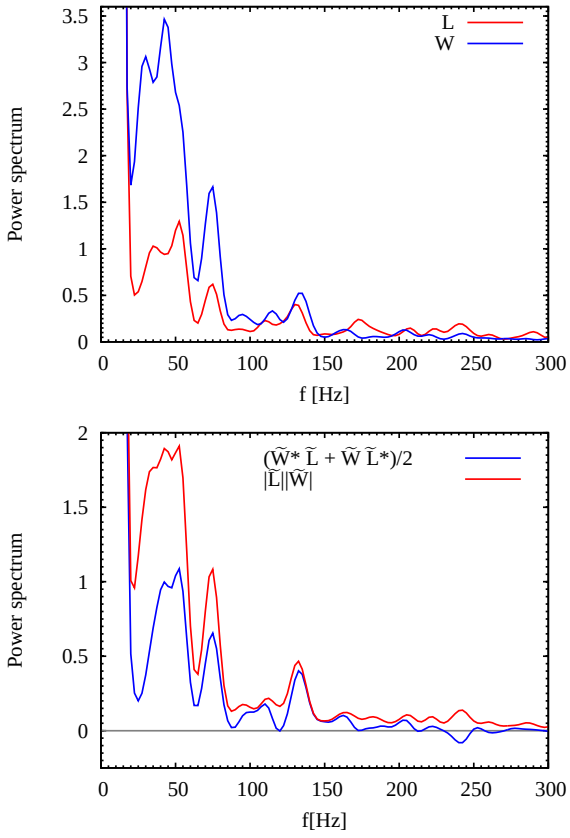

FIG. 10: Smoothed power spectrum of luminosity (L) and spectral energy ($W = E^2_{\rm rms}$) fluctuations for the model with Lattimer and Swesty EoS. L and W were normalized to their respective average values over the 274–400 ms interval. *Top:* Power spectra of L (red, lower curve) and W (blue, higher curve). *Bottom:* $|\tilde{L}|\,|\tilde{W}|$ as a red line and correlation function $\frac{1}{2}(\tilde{W}^*\tilde{L} + \tilde{W}\tilde{L}^*)$ as a blue line.

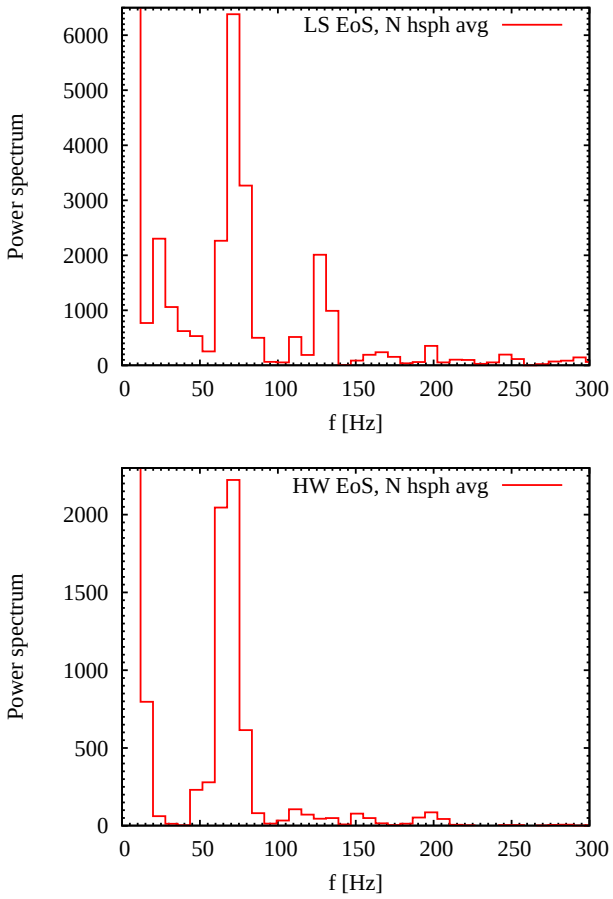

FIG. 11: Power spectra of the IceCube rate without flavor oscillations for the northern hemispheric averages, taken for the 274–400 ms post bounce interval. Because of the reduced integration time, the shot noise level of the IceCube dark current is now at 30.26. *Top:* Lattimer and Swesty EoS in analogy to Fig. 8. *Bottom:* Hillebrandt and Wolff EoS.

V. STIFF EQUATION OF STATE

Finally we briefly address the dependence of our results on the EoS used in the SN simulation. To this end we consider the run of Ref. [6] with the EoS of Hillebrandt and Wolff [19]. The $\bar{\nu}_e$ luminosity, rms energy and IceCube rate corresponding to our five angular wedges was shown in Fig. 4 in juxtaposition to the run with the Lattimer and Swesty EoS. In Fig. 2 we showed the $\bar{\nu}_e$ luminosity, rms energy and IceCube signal rate for the northern hemispheric average with the Hillebrandt and Wolff EoS in analogy to Fig. 1.

The figures reveal that strong fluctuations begin in earnest only at around 300 ms postbounce as already noted in Ref. [6]. Therefore, it makes little sense to compare the power spectrum over the first 400 ms of this run with the Lattimer and Swesty case. Instead we compare in Fig. 11 the power spectra of the IceCube rate for the northern hemispheric averages, taken over the 274–400 ms interval post bounce for the Lattimer and Swesty case (top panel) and the Hillebrandt and Wolff case (bottom). In other words, our signal duration is now $\tau = 126$ ms, implying a frequency spacing of 8 Hz and an increase of the shot-noise level by a factor $400/126 = 3.2$ (Appendix A).

Both cases show strong power with a frequency of around 70 Hz which is also visible to the naked eye in the time evolution (lower panel of Fig. 2), although the power is larger in the Lattimer and Swesty case. The signal time variations for the stiffer EoS would be plainly visible with similar significance as for the softer one.

We also note that the 70 Hz peak in the upper panel of Fig. 11 is much larger than in Fig. 8 (upper panel, red line). The difference between the two curves is only the analyzed signal interval. Here it is the final 126 ms of the run, in Fig. 8 the full 400 ms. If the signal was roughly stationary, the power of the peak would have to be the same. However, here we have a strong peak at 70 Hz with a much larger signal-to-noise than in Fig. 8, where in turn we have a much stronger peak at 50 Hz. In other words, the Fourier spectrum varies significantly as a function of time. The analysis of a realistic signal would involve studying subsets of the full-length signal where Fourier components can show up with much larger significance in spite of the increased shot noise relevant for a shorter integration time.

VI. IMPLICATIONS OF DETECTION

Hydrodynamical instabilities, in particular convective and SASI activity, and multi-dimensional processes are thought to be crucial ingredients of the mechanism that causes the explosion of core-collapse SNe [21, 22]. The nonradial asymmetries during the very early stages of the explosion can manifest themselves in large-scale asphericity and mixing of the SN blast (for recent 3-D models see Ref. [23]). A measurement of neutrino signal modulations and gravitational waves would provide direct evidence for these theoretical ideas and could yield much deeper insight into the strength, evolution, and role of nonradial hydrodynamic flows on the path to successful explosions. While the main focus of this paper is the experimental detectability of SASI and convective variations of the neutrino emission—at least as predicted by 2-D simulations—we briefly address possible interpretations of such a measurement.

A thorough discussion is hampered by the small number of SN models that are available for an analysis of the signal characteristics and dependence on the progenitor and core microphysics. Moreover, a conclusive theoretical assessment will require 3-D models. The present 2-D calculations can serve only for preliminary indications of what might be expected, provided 3-D models roughly confirm the 2-D results. The prominence of strong dipolar asymmetries as obtained by the lowest ($\ell = 1$ in terms of an expansion in spherical harmonics) SASI modes in

2-D has indeed been questioned on the basis of recent 3-D simulations [24]. However, these models do not include neutrino transport in a self-consistent way and only a small set of non-rotating models for special conditions was computed. Therefore, it is premature to judge the role of low-mode asymmetries in 3-D.

The peaks of the power spectrum of the neutrino signal reflect the mode pattern of the SN core activity. They are connected with temporal changes of the mass accretion rate onto the neutron star, which are either caused by SASI or by convective modulations of the infalling mass flow between shock and neutron star surface [5, 6]. Since the accretion downflows can be channeled more strongly to the northern or southern hemisphere, the hemispheric symmetry can easily be broken, and even long-lasting hemispheric asymmetries of the accretion structures and shock-expansion strength can emerge. Therefore there is no reason to expect exactly equal power spectra for both hemispheres. Even the dipolar SASI sloshing mode can develop different strengths in both hemispheres.

A causal connection of the peaks in the neutrino power spectra with global deformation modes of the shock surface and thus of the accretion flow between shock and proto-neutron star is supported by results presented in Ref. [6]. The Fourier spectra of the time-variable spherical harmonics dipole and quadrupole amplitudes of the shock position in that paper (Fig. 5, right column) exhibit maxima whose positions agree well with the lowest characteristic frequencies of the neutrino power spectra.

The corresponding 50 Hz peak of our model with Lattimer and Swesty EoS is actually a broad feature with high power (half-width) roughly between 30 Hz and 60 Hz. This feature is present in the northern, southern, and equatorial signals. In the equatorial case we identify it with the first two-hump maximum visible to the right of the low-frequency spike (Fig. 8, upper panel). This peak around 50 Hz is caused by the $\ell = 1$ SASI sloshing mode, which leads to quasi-periodic modulations of the mass accretion rate and associated neutrino emission in both hemispheres (see Ref. [6], page 485). The peak width is explained by the time-variations of the SASI frequency, its north-south differences by the lack of perfect hemispheric symmetry (cf. Fig. 3 in Ref. [6]).

The frequency of the $\ell = 1$ SASI mode depends on the sound-travel and mass-inflow times between neutron star surface and shock (see Eq. (32) in [2] and Eq. (18) in [4]) and thus mainly on the time-variable shock radius and to a lesser extent also on the continuously contracting NS radius. Roughly, when the average shock radius is large, the SASI frequency is lower, when the shock radius shrinks, the SASI frequency tends to be higher. Since the shock radius shows sizable time evolution (Fig. 4, left panel, in [6]), it is natural that the SASI peak of the time-integrated neutrino signal becomes fairly broad.

The peak with the next higher frequency of around 70 Hz is most easily explained by $\ell = 2$ (quadrupolar) SASI activity, although a strict discrimination of global shock oscillation modes from convective mass motions in the postshock layer is very difficult in the nonlinear phases of the two hydrodynamic instabilities. Both instabilities can trigger each other and therefore occur mostly simultaneously [4]. A possible connection of the ∼70 Hz power maximum with the quadrupolar SASI mode is suggested by three facts: (1) Analytic analysis and numerical experiments in the linear regime show that the frequency of the $\ell = 2$ mode is slightly higher than that of the $\ell = 1$ mode (cf. Fig. 5 in [2], Fig. 13 in [4]), but the exact frequency ratio depends strongly on the size of the SASI region (see Fig. 4 in [25]). (2) The appearance of the ∼70 Hz peak in the upper panel of Fig. 11 and relative weakness of power at lower frequencies at late times (274–400 ms) in our model with the Lattimer and Swesty EoS can be explained by the increasing power of the $\ell = 2$ shock oscillation mode, whose amplitude at these times becomes larger than that of the $\ell = 1$ mode (see the left panels of Fig. 5 in [6]). (3) The presence of the peak in the northern power spectrum but relative weakness or absence in the southern hemisphere may correspond to the hemispheric asymmetry of the quadrupolar shock deformation as visible in the panels of Fig. 4 in Ref. [6].

Local convective overturn motions in the accretion flow on smaller angular scales (corresponding to higher spherical harmonics modes) take place on shorter timescales than the global dipolar and quadrupolar mass shifts. Therefore they are the most probable explanation for the power peaks at frequences above 90–100 Hz. In particular such short-wavelength structures may exhibit considerable differences in the two hemispheres and also in the equatorial region, where long-lasting, non-stationary downdrafts develop at later post-bounce times. Differences between these directions in the neutrino power spectra at high frequencies are therefore not astonishing.

Moreover, the layer between shock and neutron star surface is generally more compact for the SN model with the Hillebrandt and Wolff EoS (cf. Fig. 4, left panel, of [6]). Therefore, the global shock-motion and accretion modes of this model have a lower amplitude and higher frequency than in the simulation with the Lattimer and Swesty EoS. It is possible that the very broad peak roughly between 60 Hz and 85 Hz in the former case (lower panel of Fig. 11) and simultaneous lack of a second strong peak at somewhat higher frequency is the result of a superposition of $\ell = 1$ and $\ell = 2$ activity. This interpretation is suggested by the presence of both modes with comparable amplitudes (Fig. 5 in [6]) and by the fact that for a compact postshock layer the characteristic frequencies of both modes become very similar as shown in Fig. 4 of Ref. [25].

SASI activity can therefore be reflected by different peaks in the neutrino power spectra, depending on the presence of different modes, the fastest growing ones and typically strongest in 2-D being those of $\ell = 1$ and $\ell = 2$. The exact frequencies of the peaks depend on the time-evolving structure of the postshock layer. The strongest SASI activity and thus most easily measurable signal features must be expected to occur in a time window of

some 100 ms just before the explosion sets in. The peaks in the power spectra of the integrated signal over this shorter period are significantly enhanced relative to the shot-noise level (compare upper panels of Figs. 8 and 11), favoring easier detection of these features.

The measurement of the neutrino luminosity modulations could thus confirm the existence of large non-radial hydrodynamical instabilities (SASI and convective overturn) around the beginning of the explosion, which would have to be strong enough to affect the neutrino emission from the accreting neutron star. Such a measurement would reveal an important component of SN physics, whose potential relevance is presently suggested only by numerical models, theoretical analysis, and indirect arguments based on the presence of ejecta asymmetries at much later stages of the evolution.

A detection of the SASI would definitely exclude the prompt explosion mechanism (which already seems to be ruled out by simulations) as well as all other explosion mechanisms that work faster than the SASI can develop in the SN core. The growth of the SASI activity to the nonlinear regime takes typically 100–200 ms after bounce [2, 4, 25], so SASI signatures would require a significantly delayed explosion as expected for the neutrino-driven mechanism. Most probably, their measurement would also exclude the magnetohydrodynamic mechanism, which could take place in rapidly rotating stellar cores and according to 2-D simulations could lead to relatively rapid explosions [26]. Conversely, a non-detection of strong SASI features in the neutrino signal is likely to disfavor the acoustic explosion mechanism [27, 28], which might initiate the blast wave as late as one second or more after core bounce. In this case the onset of the explosion would be preceded by at least a transient phase of strong SASI and convective overturn activity around the newborn neutron star. Such a phase is probably important to excite the compact remnant to the required powerful, large-amplitude dipole oscillations that yield the acoustic energy flux for launching the explosion.

Exclusion arguments of this kind can become even more powerful in the combination with gravitational-wave measurements as recently pointed out by Ott [29]. Thus gravitational waves and neutrino-emission variations could help to unravel the still heavily disputed processes that cause the explosions of massive stars.

VII. CONCLUSIONS

We have studied the signature of fast SN neutrino time variations in IceCube, a detector that would produce the largest event rate of any existing experiment. We have used the output of axially symmetric SN simulations recently produced by some of us. The SASI sloshing motion with time- and mode-dependent frequencies of about 50–100 Hz as well as smaller-scale, shorter-period convective overturns provide a strong imprint in the neutrino signal. Typically it would be visible even to the naked eye by simply inspecting the time sequence of registered Cherenkov photons. A Fourier analysis of the signal reveals a large signal-to-noise ratio that would be detectable for a SN throughout our galaxy.

The spectral power of the time-varying SN signal decreases with frequency and it depends on distance up to which frequency time variations can be detected. For a fiducial distance of 10 kpc the IceCube dark current is comparable to the SN signal. Based on our simulation, at this distance signal modulations typically could be seen up to 100–200 Hz. This conclusion is barely affected by possible flavor conversions.

The strongly dipolar nature of the SASI mode along the symmetry axis of the simulations implies that the observable signal variations strongly depend on the direction of viewing the SN. In particular, in the equatorial direction the signal variations caused by neutrinos emerging from the northern and southern hemispheres nearly cancel and in our most pessimistic example would be visible only to a distance of a few kpc. However, such directional cancelation effects likely would be smaller in a realistic 3-D situation, although the overall SASI signal might also be smaller. Moreover, the signal-to-noise for a given Fourier mode depends on the time window used for the analysis because the power spectrum varies strongly with time. It is premature to study these issues in too much detail because the available 2-D simulations as well as the approximations used in the neutrino transport provide only a first glance of what might be expected from a more realistic treatment.

The event rate fluctuations in IceCube are caused by fluctuations of the luminosity and of the neutrino energies, the latter being the more important effect. Therefore, in a detector with spectral information such as a water Cherenkov detector additional information can be extracted. A future megaton-class detector will have a neutrino event rate comparable to IceCube's and thus would offer significant additional capabilities through its event-by-event spectral sensitivity.

Our main message is that IceCube and future large-scale detectors can measure intriguing time-dependent features of the neutrino signal of a future galactic SN, allowing one to observe the SASI activity with neutrinos in situ, if our 2-D model is roughly representative for a more realistic treatment. Such signatures would provide a crucial test of our theoretical understanding of the core collapse phenomenon. The secular evolution of the signal as well as its fast variations may hold information, for example on the growth time of large-scale non-radial asymmetries in the SN core, the SN explosion mechanism, and the contraction behavior of the nascent NS and thus on the nuclear equation of state, but once more it is premature to forecast generic signatures on the basis of our 2-D models. Moreover, the spectral range that can be probed strongly depends on the SN distance—a fiducial case at 10 kpc may not be representative if the SN is much closer or much further away.

The excellent time resolution of IceCube can be used in

other ways. For example, the signal onset and therefore bounce time can be pinned down very well, allowing for correlations with gravitational wave detectors [12]. On the more exotic side, a possible QCD phase transition can produce a short $\bar{\nu}_e$ burst that could be detected with high significance [30].

In summary, among existing SN detectors IceCube has unique capabilities to measure fast signal variations. Identifying such features with additional spectral information is a powerful motivation to build a megaton water Cherenkov detector.

Acknowledgments

We acknowledge partial support by the DFG (Germany) under grant TR-27 "Neutrinos and Beyond," the Cluster of Excellence "Origin and Structure of the Universe," and the NSF under Grant No. PHY-0854827. We acknowledge computer time grants at the John von Neumann Institute for Computing (NIC) in Jülich, the Höchstleistungsrechenzentrum of the Stuttgart University (HLRS) under grant number SuperN/12758, the Leibniz-Rechenzentrum München, and the RZG in Garching. T.L. thanks the MPI Physics for hospitality while this work was begun. We thank the participants of the workshop JIGSAW 2010 (22–26 February 2010, Mumbai, India) for comments and discussions, in particular Timo Griesel and Thomas Kowarik.

Appendix A: Shot noise in IceCube and Fourier Transform of binned data

To estimate the shot noise of the IceCube signal we consider a signal consisting of a sequence t_j of N measured arrival times. They sample the rate $R(t)$ over the signal duration τ. The Fourier transform is

$$g(f) = \int_0^\tau \mathrm{d}t\, R(t)\, \mathrm{e}^{-\mathrm{i}2\pi f t} = \sum_{j=1}^{N} \mathrm{e}^{-\mathrm{i}2\pi f t_j} \tag{A1}$$

with the spectral power $G(f) = |g(f)|^2$. The detection rate has units of inverse time, so the Fourier components are dimensionless and $g(0) = N$ and $G(0) = N^2$. The finite-time Fourier transform is limited to the discrete frequencies $f_k = k\Delta f = k/\tau$. It is understood that a frequency f stands for a member of this discrete set.

If the sequence of events samples a uniform distribution on the interval $0 \le t_j \le \tau$, the sum in Eq. (A1) represents a random walk in the complex plane with unit step size. One concludes that an ensemble average for $G(f)$ is independent of frequency for $f \neq 0$ and follows the normalized distribution $p(G) = N^{-1}\, \mathrm{e}^{-G/N}$ [31]. The average is $\langle G\rangle = N$ so that

$$\frac{\langle G_{f\neq 0}\rangle}{G_{f=0}} = \frac{1}{N}\,. \tag{A2}$$

Usually we will include a window function $w(t)$ on the interval $0 \le t \le \tau$ to suppress edge effects on the Fourier transform. Therefore, we actually use

$$g(f) = \int_0^\tau \mathrm{d}t\, w(t)\, R(t)\, \mathrm{e}^{-\mathrm{i}2\pi f t}\,. \tag{A3}$$

The average weight must be unity, implying

$$\int_0^\tau \frac{\mathrm{d}t}{\tau}\, w(t) = 1\,. \tag{A4}$$

Fourier components that vary fast on the scale τ are returned with their original amplitude.

We determine the impact of a window function on the shot noise by extending the picture of a random walk in the complex plane to a variable step size. The different random walks must be combined in quadrature and the expectation value is modified as

$$\langle G\rangle = \langle w^2\rangle\, N \tag{A5}$$

where

$$\langle w^2\rangle = \int_0^\tau \frac{\mathrm{d}t}{\tau}\, w^2(t)\,. \tag{A6}$$

We will specifically use the Hann window

$$w(t) = 1 - \cos(2\pi\, t/\tau)\,, \tag{A7}$$

implying that the shot-noise power increases by a factor

$$\langle w^2\rangle = \frac{3}{2}\,. \tag{A8}$$

Next we translate this result to the appropriate normalization for our Fourier transform. If we have $N_{\rm bins}$ bins of equal width $\Delta = \tau/N_{\rm bins}$, and the signal rate $R(t)$, the Fourier transform of this rate sampled at times $t_j = j\,\Delta$ with $j = 0, \ldots, N_{\rm bins} - 1$ is

$$h(f_k) = \Delta \sum_{j=0}^{N_{\rm bins}-1} R(t_j)\, \mathrm{e}^{\mathrm{i}2\pi t_j k\delta f}\,. \tag{A9}$$

The frequencies are $f_k = k/\tau = k\delta f$ with $k = 0, \ldots, N_f$ and $N_f = f_{\rm max}/\delta f$. Here $f_{\rm max} = 1/2\Delta$ is the Nyquist frequency. Since $\delta f = 1/\tau$ we have $N_f = N_{\rm bins}/2$.

In practice our data are provided for a duration $\tau = 400$ ms so that $\delta f = 2.5$ Hz. We use 1 ms sampling and thus consider $\Delta = 1$ ms bins, providing a Nyquist frequency of $f_{\rm max} = 500$ Hz as an upper cutoff. For $f = 0$ and $f_{\rm max}$ the spectral power is respectively defined as

$$P(0) = \frac{|h(0)|^2}{N_{\rm bins}^2} \quad \text{and} \quad P(f_{\rm max}) = \frac{|h(f_{\rm max})|^2}{N_{\rm bins}^2}\,. \tag{A10}$$

For all other frequencies we define

$$P(f_k) = \frac{|h(f_k)|^2 + |h(-f_k)|^2}{N_{\rm bins}^2} = 2\,\frac{|h(f_k)|^2}{N_{\rm bins}^2}\,. \tag{A11}$$

The second equality applies because the transformed function is real and therefore $|h(-f)|^2 = |h(f)|^2$.

Using a signal duration $\tau = 400$ ms and Eq. (4) for the background rate we find: $N_{\rm bkgd} = 5.4 \times 10^5$ and $h(0) = N_{\rm bkgd}$. The ratio $|h(f_k)|^2/|h(0)|^2$ was earlier found to be $1/N_{\rm bkgd}$ times a factor 3/2 if we use the Hann window. Our definition of power for binned data involves a factor $2/N_{\rm bins}^2$. Therefore, we find for the IceCube shot noise, relevant for a signal duration of 400 ms and a Hann window,

$$P_{\rm shot} = \frac{3}{2}\,\frac{N_{\rm bkgd}^2}{N_{\rm bkgd}}\,\frac{2}{N_{\rm bins}^2} = \frac{3N_{\rm bkgd}}{N_{\rm bins}^2} = 10.08\,. \qquad \text{(A12)}$$

We have confirmed this result with a few numerical Monte Carlo realizations.

If we use a subset of the full data, i.e. a shorter signal duration τ with correspondingly fewer bins, the frequency spacing is increased, but the power at a given frequency remains the same except for detailed changes implied by the reduced data. Both $N_{\rm bkgd}$ and $N_{\rm bins}$ get reduced linearly with τ and therefore $P_{\rm shot} \propto \tau^{-1}$. The signal-to-noise of spectral power in a stationary signal increases linearly with integration time.

[1] J. M. Blondin, A. Mezzacappa and C. DeMarino, "Stability of standing accretion shocks, with an eye toward core collapse supernovae," Astrophys. J. **584**, 971 (2003) [astro-ph/0210634].

[2] N. Ohnishi, K. Kotake and S. Yamada, "Numerical analysis on standing accretion shock instability with neutrino heating in the supernova cores," Astrophys. J. **641**, 1018 (2006) [astro-ph/0509765].

[3] T. Foglizzo, P. Galletti, L. Scheck and H.-T. Janka, "Instability of a stalled accretion shock: Evidence for the advective-acoustic cycle," Astrophys. J. **654**, 1006 (2007) [astro-ph/0606640].

[4] L. Scheck, H.-T. Janka, T. Foglizzo and K. Kifonidis, "Multidimensional supernova simulations with approximative neutrino transport. II. The advective-acoustic cycle in the supernova core," Astron. Astrophys. **477**, 931 (2008) [arXiv:0704.3001].

[5] A. Marek and H.-T. Janka, "Delayed neutrino-driven supernova explosions aided by the standing accretion-shock instability," Astrophys. J. **694**, 664 (2009) [arXiv: 0708.3372].

[6] A. Marek, H.-T. Janka and E. Müller, "Equation-of-state dependent features in shock-oscillation modulated neutrino and gravitational-wave signals from supernovae," Astron. Astrophys. **496**, 475 (2009) [arXiv:0808.4136].

[7] C. D. Ott, A. Burrows, L. Dessart and E. Livne, "2D multi-angle, multi-group neutrino radiation hydrodynamic simulations of postbounce supernova cores," Astrophys. J. **685**, 1069 (2008) [arXiv:0804.0239].

[8] S. Hannestad, A. Mirizzi, G. G. Raffelt and Y. Y. Y. Wong, "Neutrino and axion hot dark matter bounds after WMAP-7," [arXiv:1004.0695].

[9] G. Drexlin, "Direct neutrino mass measurements," J. Phys. Conf. Ser. **136**, 022031 (2008)

[10] A. S. Dighe, M. T. Keil and G. G. Raffelt, "Detecting the neutrino mass hierarchy with a supernova at IceCube," JCAP **0306**, 005 (2003) [hep-ph/0303210].

[11] T. Kowarik, T. Griesel and A. Piegsa (for the IceCube Collaboration), "Supernova search with the AMANDA/ IceCube detectors," [arXiv:0908.0441].

[12] F. Halzen and G. G. Raffelt, "Reconstructing the supernova bounce time with neutrinos in IceCube," Phys. Rev. D **80**, 087301 (2009) [arXiv:0908.2317].

[13] M. Rampp and H.-T. Janka, "Radiation hydrodynamics with neutrinos. Variable Eddington factor method for core collapse supernova simulations," Astron. Astrophys. **396**, 361 (2002) [astro-ph/0203101].

[14] R. Buras, M. Rampp, H.-T. Janka and K. Kifonidis, "Two-dimensional hydrodynamic core-collapse supernova simulations with spectral neutrino transport. I. Numerical method and results for a 15 $M_\odot$ star," Astron. Astrophys. **447**, 1049 (2006) [astro-ph/0203101].

[15] A. Marek, H. Dimmelmeier, H.-T. Janka, E. Müller and R. Buras, "Exploring the relativistic regime with Newtonian hydrodynamics: an improved effective gravitational potential for supernova simulations," Astron. Astrophys. **445**, 273 (2006) [astro-ph/0203101].

[16] B. Müller, H.-T. Janka and H. Dimmelmeier, "A new multi-dimensional general relativistic neutrino hydrodynamics code for core-collapse supernovae. I. Method and code tests in spherical symmetry," [arXiv:1001.4841].

[17] S. E. Woosley and T. A. Weaver "The evolution and explosion of massive stars. II. Explosive hydrodynamics and nucleosynthesis," Astrophys. J. Suppl. **101**, 181 (1995).

[18] J. M. Lattimer and F. D. Swesty "A generalised equation of state for hot, dense matter," Nucl. Phys. A **535**, 331 (1991).

[19] W. Hillebrandt and R. G. Wolff, in Nucleosynthesis: Challenges and New Developments, ed. W. D. Arnett and J. W. Truran (Univ. Chicago Press, 1985), p. 131.

[20] A. Mirizzi, G. G. Raffelt and P. D. Serpico, "Earth matter effects in supernova neutrinos: Optimal detector locations," JCAP **0605**, 012 (2006) [astro-ph/0604300].

[21] H.-T. Janka, K. Langanke, A. Marek, G. Martínez-Pinedo and B. Müller, "Theory of core-collapse supernovae," Phys. Rept. **442**, 38 (2007) [astro-ph/0612072].

[22] A. Burrows, L. Dessart, C. D. Ott and E. Livne, "Multi-dimensional explorations in supernova theory," Phys. Rept. **442**, 23 (2007) [astro-ph/0612460].

[23] N. J. Hammer, H.-T. Janka and E. Müller, "Three-dimensional simulations of mixing instabilities in supernova explosions," Astrophys. J. **714**, 1371 (2010) [arXiv:0908.3474].

[24] J. Nordhaus, A. Burrows, A. Almgren and J. Bell, "Dimension as a key to the neutrino mechanism of core-collapse supernova explosions," Astrophys. J., in press (2010) [arXiv:1006.3792].

[25] J. M. Blondin and A. Mezzacappa, "The spherical accretion shock instability in the linear regime," Astrophys. J. **642**, 401 (2006) [astro-ph/0507181].

[26] A. Burrows, L. Dessart, E. Livne, C. D. Ott and J. Murphy, "Simulations of magnetically driven supernova and

hypernova explosions in the context of rapid rotation," Astrophys. J. **664**, 416 (2007) [astro-ph/0702539].

[27] A. Burrows, E. Livne, L. Dessart, C. Ott and J. Murphy, "A new mechanism for core-collapse supernova explosions," Astrophys. J. **640**, 878 (2006) [astro-ph/0510687].

[28] A. Burrows, E. Livne, L. Dessart, C. D. Ott and J. Murphy, "Features of the acoustic mechanism of core-collapse supernova explosions," Astrophys. J. **655**, 416 (2007) [astro-ph/0610175].

[29] C. D. Ott, "The gravitational wave signature of core-collapse supernovae," Class. Quant. Grav. **26**, 063001 (2009) [arXiv:0809.0695].

[30] B. Dasgupta, T. Fischer, S. Horiuchi, M. Liebendörfer, A. Mirizzi, I. Sagert and J. Schaffner-Bielich, "Detecting the QCD phase transition in the next Galactic supernova neutrino burst," Phys. Rev. D **81**, 103005 (2010) [arXiv:0912.2568].

[31] A. S. Dighe, M. T. Keil and G. G. Raffelt, "Identifying earth matter effects on supernova neutrinos at a single detector," JCAP **0306**, 006 (2003) [hep-ph/0304150].